Nuclear Engineering and Technology 57 (2025) 103164

Contents lists available at ScienceDirect

Nuclear Engineering and Technology

journal homepage: www.elsevier.com/locate/net

Original Article

High-power performance studies of an S-band high-gradient accelerating cavity for medical applications☆

P. Martinez-Reviriego [a],*, N. Fuster-Martínez [a],*, D. Esperante [a,b], M. Boronat [a], B. Gimeno [a], C. Blanch [a], D. González-Iglesias [a], P. Martín-Luna [a], E. Martínez [a], A. Menendez [a,b], L. Pedraza [a], J. Fernández [a], J. Fuster [a], A. Grudiev [c], N. Catalan Lasheras [c], W. Wuensch [c]

[a] Instituto de Fisica Corpuscular (CSIC-University of Valencia), Carrer del Catedrátic José Beltrán Martinez, 2, Paterna, 46980, Valencia, Spain
[b] Electronics Engineering Department, University of Valencia, Avinguda de l'Universita, Burjassot, 46100, Valencia, Spain
[c] CERN, Esplanade des particules, 1, Meyrin, 1211, Switzerland

ARTICLE INFO

Keywords:
High-gradient RF cavities
Linac
Hadron therapy

ABSTRACT

High-Gradient accelerating cavities are one of the main research lines in the development of compact linear accelerators. However, the operation of such accelerating cavities is currently limited by non-linear electromagnetic effects that are intensified at high electric fields, such as RF breakdowns, dark currents and radiation. A novel normal-conducting High Gradient S-band Backward Travelling Wave accelerating cavity for medical application (v = 0.38c) has been designed and constructed at CERN with a design gradient of 50 MV/m. In this paper, the high-power performance studies of this novel design carried out at the IFIC high-power laboratory are presented, as well as the analysis of the conditioning parameters in combination with numerical simulations.

1. Introduction

Radiotherapy is a cancer treatment in which radiation is used to kill tumour cells. The most extended radiation used nowadays is X-rays due to the fact that they are more penetrating than electrons and easier and cheaper to produce than other types treatments involving heavier particles. However, hadron beams (typically protons and C^{6+} ions) have the advantage of exhibiting a very localised energy deposition in comparison to the conventional radiotherapy with X-rays [1]. The dose deposition by this type of radiation is described by the Bragg peak and can minimise the dose to normal tissue and nearby critical organs. This is considered particularly valuable for paediatric cases, as for about 25% of tumour types, children are more sensitive to the adverse effects of radiation [2]. Furthermore, therapies with C^{6+} ions have a greater radiobiological efficiency than X-rays and protons by a factor 3–4 [3], making it possible to reduce the number of treatment sessions, which could reduce the cost of such treatments and the patients discomfort, as well as to treat radio-resistant tumours.

Over the last two decades, the therapies with protons have gained a huge momentum, mainly based on synchrotrons and cyclotrons [4]. However, high frequency linac (Linear Accelerator) solutions are being investigated as a promising new technology that could herald new cancer treatment options with the advantage of modularity and speed in the control of the beam energy [5–7]. A linac is composed of a chain of accelerating cavities, that can be individually controlled, allowing to change the energy of the final beam pulse-to-pulse (within 2–5 μs, whereas for cyclotrons it takes 80–100 ms and for synchrotrons 1–2 s). This makes linacs highly suited for short therapy sessions and treating moving organs. For protons, a first linac solution of approximately 28 m length based on a Coupled Cavity Linac (25 MV/m) achieved proton beams with energies of 230 MeV in September 2022 (TOP-IMPLART in Italy and AVO-ADAM in London and Cyprus) [8,9]. For C^{6+} ions, the required accelerator technology is more complex due to the need to reach higher energies than for protons for the same equivalent penetration depth (430 MeV/u compared to 230 MeV/u for protons) [5], and the lower charge-over-mass ratio, that affects the acceleration efficiency. There are very few facilities in the world (in Europe only 5 operational centres and one under construction) based on synchrotrons [4]. Research studies are being made by the scientific community to develop a new generation of ion therapy accelerators that are more compact and efficient, increasing the accessibility to these

☆ Work supported by Ministerio de Universidades (Gobierno de España) under grant number FPU19/00585 and Generalitat Valenciana, Spain CDEIGENT/2021/012.

* Corresponding authors.
E-mail addresses: pablo.martinez.reviriego@ific.uv.es (P. Martinez-Reviriego), nuria.fuster.martinez@ific.uv.es (N. Fuster-Martínez).

https://doi.org/10.1016/j.net.2024.08.033
Received 22 June 2024; Received in revised form 13 August 2024; Accepted 16 August 2024
Available online 19 August 2024

therapies [10]. Currently, the most promising solutions for C^{6+} ions, are a high frequency linac or a superconducting synchrotron. In this case, as a consequence of the lower ratio charge over mass of the ions and the need of reaching higher energies (up to 430 MeV/m) compared with protons (up to 230 MeV), the number of accelerating cavities increases, as well as the length and cost of the accelerator. In this paper, we will focus on the high frequency linac option, which is still in a conceptual and R&D phase [11].

The HG-RF technology has the potential of reducing the linac length for both protons and ions by a factor 2–3, which justifies the investigation of its use and limitations. This technology was originally developed for high-energy particle colliders, mainly within the framework of the CLIC project at CERN [12]. Remarkable advances have been made in the last decade, reaching accelerating gradients on the order of 100 MV/m to accelerate electrons [13]. Currently, the maximum achievable accelerating gradient is limited by the formation of non-linear electromagnetic (EM) phenomena such as RF breakdowns (BDs) and field emission [14], which can damage the accelerating cavities, affect their efficiency, as well as generate intolerable background radiation. The RF BDs generate electric discharges, that are originated in the nano-protrusions on the metallic walls of the cavity, due to the spontaneous emission of electrons (dark current) by the so-called field emission effect [15]. This occurs where the RF electric fields are more intense [16]. The phenomenology of BDs is a very complex field involving studies in RF [17], material science [18,19] and plasma physics [20]. Most of the models and empirical criteria to explain these phenomena have become obsolete after showing a clear inconsistency with the latest experimental results for accelerating gradients in the order of tens of MV/m. Experiments validated by simulations are crucial for a better understanding of these phenomena through characterising the dark current beam dynamics and determining the conditions favouring its formation in new accelerating cavity designs [21,22]. Another HG-RF technological challenge is related to the increase of power consumption, which has a squared dependence on the accelerating gradient. Therefore, cost studies considering both, construction and operational issues are essential also to understand the possible limitations and push forward the use of this technology.

Two normal-conducting HG S-band (2.9985 GHz) Backward Travelling Wave (BTW) accelerating cavities for low energy hadrons (β = 0.38) were designed and constructed by the TERA Foundation and CERN [23]. The cavity was designed for an accelerating gradient of 50 MV/m. However, experiments carried out at CERN with the accelerating structure installed in the reverse position demonstrated that gradients of 80 MV/m are attainable [24]. However, due to the lack of longitudinal periodicity of the structure, the fields distribution inside the structure was not uniform. In addition, a 15 cells HG 2.856 GHz negative harmonic accelerating waveguide for $\beta = 0.3$ was tested up to 50 MV/m by RadiaBeam, in collaboration with the Argonne National Laboratory [25]. The conditioning process was operated at a repetition rate of 30 Hz and the BDR reached was 10^{-3} BD per pulse (bpp).

In this paper, we present the first high-power tests performed on the second innovative BTW RF accelerating cavity prototype, installed for the first time in the operational position for acceleration. The repetition rate of the experiment reached 300 Hz, which is factor 10 higher than the previous experiments at S-band. In addition, experimental measurements showing the evolution of the beta enhancement factor with the conditioning and evidence of the correlation between the BD probability and the shape of the incident pulse are shown. Moreover, the BTW accelerating structure dark currents and radiation formation have been modelled with a 3D EM code and validated experimentally. These results are essential for understanding the shielding requirements of this kind of facilities. In Section 2, the experimental set-up at the IFIC high power laboratory and the BTW RF cavity specifications are described. Section 3 presents the results of the high power tests performed. This section includes the description of the conditioning process and the characterisation of the non-linear EM phenomena

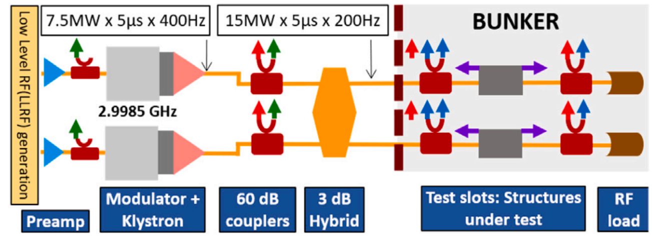

Fig. 1. IFIC high-power laboratory layout and main parameters.

Fig. 2. IFIC high-power facility.

formation during this process. In Section 4, we present a 3D EM model developed using the commercial software CST-PS to study the dark current beam dynamics in the BTW RF cavity design. The predictions of this model are validated through dedicated measurements. Finally, in Section 5, the main conclusions from these studies are presented.

2. The IFIC high power RF laboratory

The IFIC HG-RF laboratory was designed and built to perform HG R&D of normal conducting S-band RF components.

The high-power (HP) system layout is very similar to the one at the Xbox-3 test facility at CERN operated at 12 GHz [26], but for a central frequency of 2.9985 GHz. The low level RF (LLRF) control system is based on a real-time Ni-PXI architecture and the HP system is able to amplify the RF signal up to a design peak power of 15 MW. The main components of the HP system are the two modulators, the two klystrons and the RF wave guide system, which guides the RF pulses to the device under test (DUT), e.g. accelerating cavity to be tested. The laboratory has two lines for testing and can operate to a maximum operational frequency rate of 400 Hz if only one DUT is being tested. If two DUTs are being tested, the maximum operational frequency rate is 200 Hz. The layout and main operational parameters of the HP system are illustrated in Fig. 1 and more details can be found in [27]. A picture of the IFIC high-power laboratory is shown in Fig. 2, where one of the two modulators and klystrons can be seen along with the concrete bunker containing the DUT used for radiation protection reasons. The laboratory was commissioned in June 2019 and in October 2019 started the testing of the first HG accelerating RF cavity.

2.1. The BTW S-band cavity

In order to investigate the use of the high-gradient technology in hadron therapy based on linacs, an S-band BTW accelerating structure was designed and two prototypes were constructed at CERN, funded by the CERN Knowledge Transfer (KT) unit [24]. This BTW is designed to accelerate a hadron beam with β = 0.38; for protons, this corresponds

Table 1
BTW RF accelerating cavity main parameters.

Parameter (unit)	Value
Frequency (GHz)	2.9985
Phase advance per cell (rad)	$5\pi/6$
Phase velocity	0.38c
Pulse width (μs)	2.5
Average accelerating field (MV/m)	50
Number of cells	12
Structure length (mm)	189.9
Quality factor (first/last cell)	6954/7415
Normalised shut impedance (MΩ/m)	51.5/54.6
Filling time (ns)	224
Group velocity (first/last cell) (%c)	0.39/0.21
Peak input power (MW)	20.6
Max S_c/E_a^2 (A/V)	3.1×10^{-4}
Max E_s (MV/m)	219

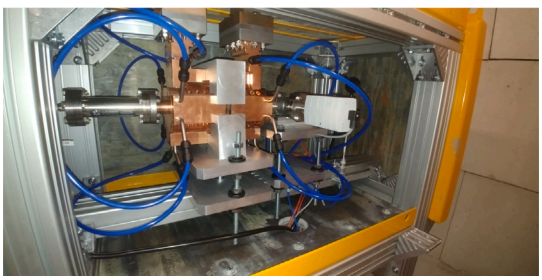

Fig. 3. BTW accelerating cavity installed at the IFIC high-power test stand.

Table 2
Main conditioning operational parameters.

Parameter (unit)	2019	2020	2021a	2021b
Operation (days)	16	6	80	17
Operation (pulses [$\times 10^6$])	8	8.5	363	574
Operation during night	Never	Sometimes	Sometimes	Always
Repetition rate	100	100	100	300
Rise pulse length (ns)	100	100	100	100
Fall pulse length (ns)	100	100	300	300
Flat-top pulse length (ns)	550	400	200	200/500/800
Chiller water Temperature (°)	22	22	22	22–25

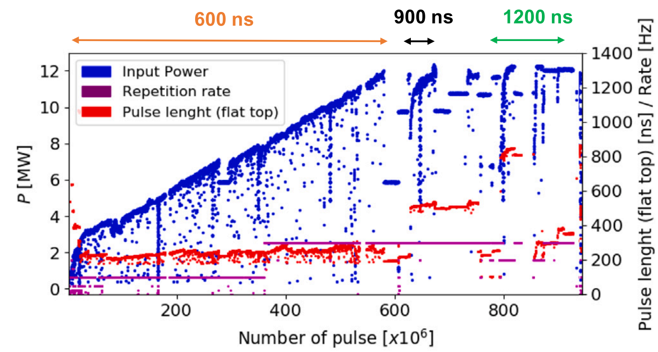

Fig. 4. Conditioning process of the S-Band BTW accelerating cavity with input power, repetition rate and flat-top pulse length in different colours on the top of the figure indicated as a function of the pulse number. (For interpretation of the references to colour in this figure legend, the reader is referred to the web version of this article.)

to an energy of 76 MeV, which is the lowest energy planned for the linac-mounted gantry of the TULIP (turning linac for proton therapy) design facility (see Table 1). The designed accelerating gradient of the cavity is 50 MV/m but it was reduced to 40 MV/m to fulfil the medical requirements [7].

In Fig. 3, the BTW installed in the IFIC high-power test stand is illustrated. As can be seen, the accelerating structure is surrounded by diagnostics used to measure and characterise the non-linear EM phenomena such as directional couplers to measure the incident, reflected and transmitted power signals to the DUT, Faraday Cups (FC) to measure the dark current and an ionisation gas detector to monitor the radiation during the tests.

3. High power RF tests

Due to the intensified generation of non-linear EM phenomena in HG conditions such as field emission, electromagnetic vacuum arcs, a fresh structure that has undergone the entire fabrication process of machining, assembly and cleaning is not capable of sustaining HG fields from the beginning of operation. Therefore, a process of high-power conditioning is needed for the structure to adapt to HG pulses. In this process, the input power into the DUT is increased in steps while keeping the BD rate (BDR) constant to gradually a pre-defined value. This process can take several months, depending on the RF cavity design and on the operational parameters.

In this section, we present the conditioning process performed at the IFIC high-power laboratory on one of the two S-band BTW accelerating cavity prototypes. In addition, the characterisation and evolution of the main non-linear EM phenomena during this process are analysed and discussed.

3.1. Conditioning

The conditioning process of the BTW accelerating cavity prototype at IFIC started in June 2019. A fixed BDR limit was set to 3×10^{-5} bpp and the vacuum level was kept below an acceptable threshold of 3×10^{-7} mbar.

During the 2019 conditioning the input power was increased manually and the total pulse length was set to 750 ns with a symmetric rise and fall length of 100 ns.

In 2020, the operation of the laboratory could not be started until October due to the COVID-19 outbreak. In October 2020, the conditioning procedure resumed using the conditioning algorithm developed for the CLIC X-band accelerating structures in the X-boxes at CERN, adapted to work with the specific hardware of the IFIC laboratory. In addition, due to the slow progress of the conditioning process, it was decided to reduce the pulse length to a total value of 600 ns with a symmetric rise and fall value of 100 ns each. In 2021, the pulse shape was modified to reduce the reflected power to the klystrons by keeping the total pulse length to the same value but changing the fall time to 300 ns. Moreover, in 2021, a new operational mode was implemented, where all the pulses generated by the RF system were sent to the line where the accelerating cavity under test was installed. This allowed the system to work at 300 Hz instead of 100 Hz, making the process 3 times faster. In order to take into account this modification, the operational periods in 2021 are divided in two blocks. The first block (2021a) corresponds to the conditioning performed at 100 Hz, and the second (2021b) to the period operating at 300 Hz. A summary of the main operational parameters used in the different mentioned periods is presented in Table 2.

A summary of the conditioning process is shown in Fig. 4 where the input power, repetition rate and flat-top pulse length are plotted. Note that the regions with constant input power correspond to periods of time when BDR measurements were carried out. Those measurements involve operating at constant gradient for a large number of pulses and counting the amount of BDs produced. The BDR measurement indicates the confidence level of performance.

In order to compute the accelerating gradient for a given input power the following relation (1) is used [28],

$$G\ [\text{MV/m}] = 50\ [\text{MV/m}]\sqrt{\frac{P_{in}\ [\text{MW}]}{20.16\ [\text{MW}]}}, \tag{1}$$

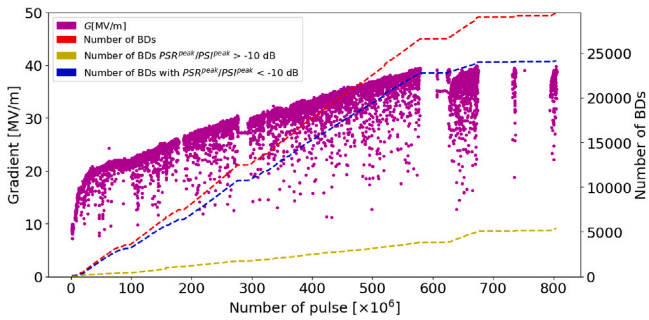

Fig. 5. History plot of gradient and cumulative number of BDs. (For interpretation of the references to colour in this figure legend, the reader is referred to the web version of this article.)

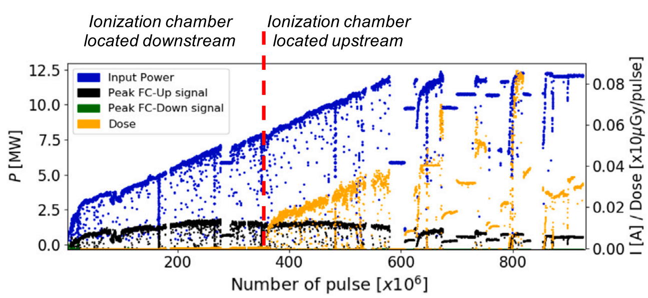

Fig. 6. Input power in blue, downstream FC in green, upstream FC in black and radiation dose from the ionisation chamber in yellow as a function of the RF pulse number during the BTW conditioning process. (For interpretation of the references to colour in this figure legend, the reader is referred to the web version of this article.)

A maximum accelerating gradient of 39 MV/m was reached for the maximum power available at the high-power sources with a pulse length of 1.2 μs. This is more than a factor 2 higher than the CCL cavities used by the AVO-ADAM high frequency linac design for protontherapy (16.5 MV/m) for this beta [8]. In Fig. 5 the gradient as a function of the number of pulses is illustrated, as well as the accumulated number of BD.

Note that the straight line of the cumulative number of BDs indicates good performance of the conditioning algorithm. It was observed that most of the measured BDs have a small amount of reflected power. In Fig. 5, the accumulated number of BDs with an integrated reflected signal above and below 10 dBs are indicated in yellow and blue, respectively. The observed gaps correspond to days when other tests were performed, such as the calibration of power signals, radiation scans and BDR measurements.

In addition, dark current and radiation measurements were performed along with the conditioning process. The results of these measurements are shown as a function of the number of RF pulses in Fig. 6. In this plot, the measured signal from the input power is shown in blue, the downstream FC in green, the upstream FC in black, and the radiation dose from the ionisation chamber in yellow, as depicted in the set-up in Fig. 3.

Due to the cavity's low phase velocity, dark current electrons are collected in the upstream FC, whereas they do not reach the downstream FC. This is in agreement with CST results shown in Section 4. Because of this observation, the ionisation chamber used to measure the photon equivalent dose was moved next to the upstream FC. As shown in Fig. 6, the signal measured at the upstream FC reaches a plateau during the conditioning process. In contrast, the radiation dose level keeps increasing throughout the conditioning process since at higher input power, the dark current electrons reach higher kinetic energy.

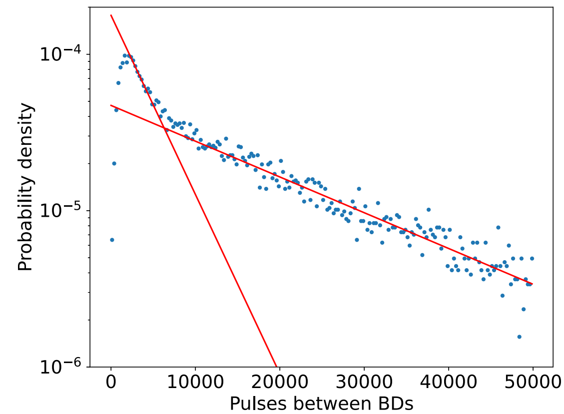

Fig. 7. Probability density of the interval between two consecutive BDs against the number of pulses between consecutive BDs. Blue points: experimental data. Red lines: double-exponential fit.

3.2. Conditioning parameters analysis

In the following, we present a detailed analysis of some parameters characterising the conditioning process.

The distribution of time intervals between BDs was fitted to a double exponential, as shown in Fig. 7. The presence of two distributions implies that the BDR is enhanced for a certain period after a BD before returning to the expected BDR [14]. This suggests the tendency for BDs to occur temporally in clusters, likely due to craters formed created on the surface after a BD. Eventually, the BDR returns to its original value because of the conditioning effect. The existence of a local maximum is a consequence of the conditioning algorithm, which turns off and gradually ramps up the power after a BD occurs to avoid damage to the structure.

Furthermore, the dark current as a function of the input power was measured for different steps in the conditioning process. This allowed to study the evolution of the enhancement factor β_e in the Fowler–Nordheim model describing the field emission as [29],

$$\frac{d\log_{10}(I/E_0^{2.5})}{d(1/E_0)} = -\frac{G\phi^{3/2}}{\beta_e}, \tag{2}$$

where $G = 2.84 \times 10^9$ V/m eV$^{3/2}$ is a constant, I is the measured dark current, E_0 is the surface electric field, $\phi = 4.5$ eV is the copper work function, and β_e is the enhancement factor that relates surface electric field with the value of the electric field in the spot. In Fig. 8, the two terms dependent on the dark current intensity and the accelerating voltage in Eq. (2) are plotted one against each other. The slope of the different curves provides the FN β_e factor at different points in the conditioning process.

It would be reasonable to expect β_e to decrease along the conditioning process as

$$\beta_e E_{max} = \text{constant}, \tag{3}$$

where E_{max} is the maximum accelerating field achieved at a given point of the conditioning.

In Fig. 9, a linear dependence of the beta enhancement factor as a function of the inverse of the maximum electric field reached as progressing in the conditioning process is observed.

In addition, the effect on the radiation dose normalised to pulse length and repetition rate, measured outside the cavity, was studied as a function of the conditioning process. In Fig. 10, the dose measured by the ionisation chamber located next to the upstream FC is shown as a function of the gradient at different points in the conditioning process. Each point in the conditioning process is characterised by the maximum power achieved and pulse length. Taking into account this, the blue

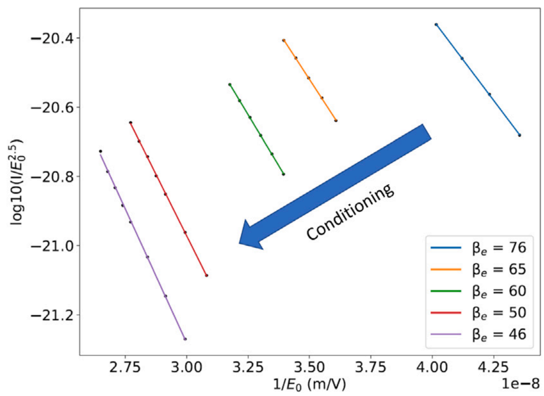

Fig. 8. Dark current and accelerating gradient dependence as the Fowler–Nordheim model for different points as we progress on the conditioning process.

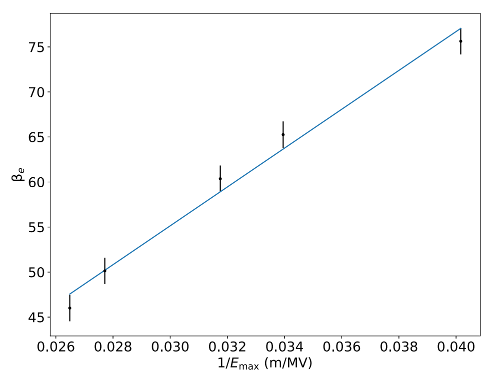

Fig. 9. β_e factor evolution as we progress on the conditioning process.

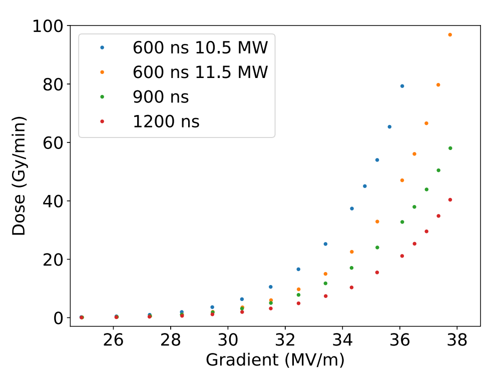

Fig. 10. Normalised measured dose to the pulse length and pulse repetition rate as a function of the accelerating gradient for different points along the conditioning process. (For interpretation of the references to colour in this figure legend, the reader is referred to the web version of this article.)

curve corresponds to 10.5 MW and 600 ns, the orange to 11.5 MW and 600 ns, the green curve to 11.5 MW and 900 ns and the red curve to 11.5 MW and 1200 ns, respectively. As shown in Fig. 10, the radiation dose, normalised to pulse length and repetition rate, decreases with the conditioning process.

Finally, the BDR was studied after reaching the maximum power that the current setup can deliver. The BDR is defined as the number of BDs per pulse and unit length, and it follows the scaling law [30],

$$BDR \propto E_{acc}^{30} \cdot \tau^{5}, \tag{4}$$

where E_{acc} is the accelerating gradient and τ the pulse length.

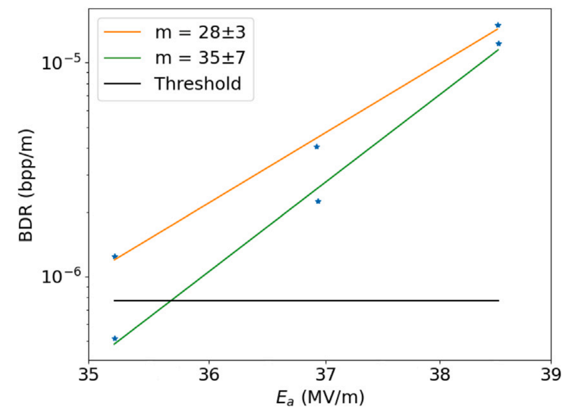

Fig. 11. BDR measurements done just after finishing the conditioning process (orange) and after 92×10^6 pulses operating at the maximum power reached (green). (For interpretation of the references to colour in this figure legend, the reader is referred to the web version of this article.)

In Fig. 11, the measured BDR for different accelerating gradients is shown. A first measurement was taken just after finishing the conditioning process and a second one after several days of conditioning at the maximum power reached.

As shown in Fig. 11, the BDR improves for the second set of measurements, which proves that conditioning of the structure keeps ongoing even operating at fixed gradient. The second set of measurements shows a gradient of 35.2 MV/m, with a BDR is below the limit required for medical applications of 7.7×10^{7} bpp/m. In addition, in both cases, the slope of the fit is consistent with the order of magnitude of Eq. (4).

The BD localisation is a typical analysis performed during the conditioning process. This analysis helps to identify hot spot regions that could interrupt the conditioning process and limit the overall performance of the structure. This analysis was carried out using the *edge method* [31], which compares the time difference between the detection of the reflected rise signal and the transmitted fall signal when a BD occurs, as shown in Eq. (5).

$$t_{edge} = \frac{t_{ref} - t_{tra}}{2}, \tag{5}$$

where t_{ref} is the rise time of the reflected signal and t_{tra} is the fall time of the transmitted signal. Afterwards, the corresponding cell number for each t_{edge} can be determined with the associated delay time to each cell,

$$t_n^{delay} = \sum_{n_{cell}}^{n_{BD}} \frac{L_{cell}}{v_g(n_{cell})}, \tag{6}$$

where L_{cell} is the length of the cell, n_{cell} ranges from 1 to 12, v_g is the group velocity of cell and n_{BD} is the cell number where the BD occurred. An example of the incident, reflected and transmitted power signal amplitudes during a BD pulse can be seen in Fig. 12.

The BD localisation distribution as a function of the cell number for all the BDs detected during the conditioning process can be seen in Fig. 13 for the different pulse lengths used in the conditioning.

A BD accumulation can be observed for cells number 8 and 9 for pulses of 600 ns length at the top of Fig. 13, whereas this accumulation disappears for longer pulses. Deeper analysis of this phenomenon showed that this accumulation was related to BDs with low reflected signal, which were observed only for short pulses. These correspond to the yellow spots in Fig. 14, where the density of pulses for the reflected power and t_{edge} is shown.

When BDs with low reflected power are filtered out from the analysis, the localisation for the short pulses shows a more uniform behaviour, as shown in Fig. 15. In this case, the accumulation of BDs observed decreases for higher cell number.

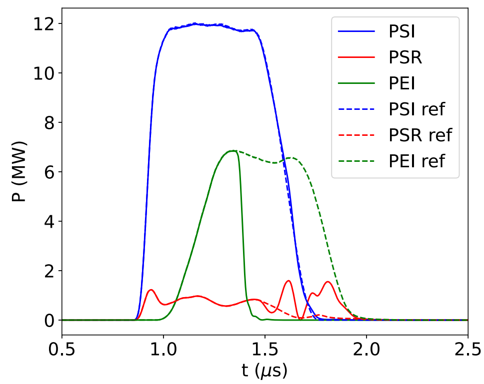

Fig. 12. Comparison between incident (PSI), reflected (PSR) and transmitted (PEI) pulse shape for a BD (solid lines) and normal event (dashed line).

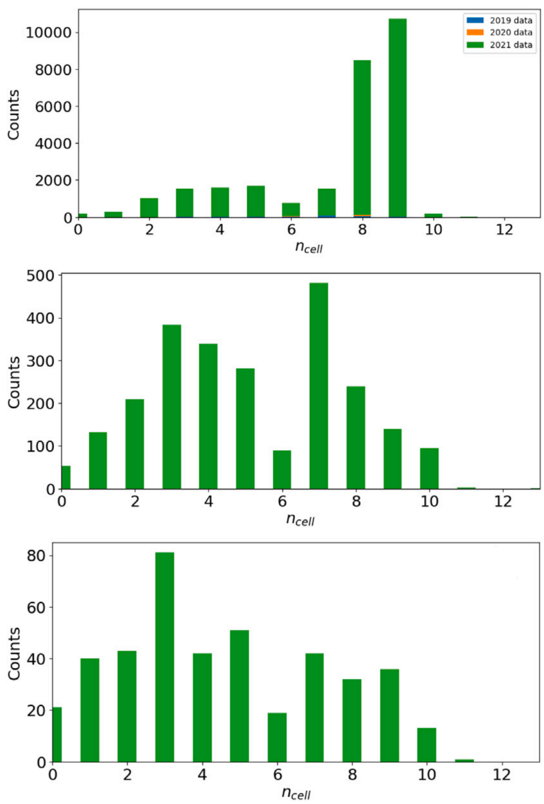

Fig. 13. BD localisation analysis for 600 ns (top), 900 ns (middle) and 1200 ns (bottom) pulse length during the conditioning process.

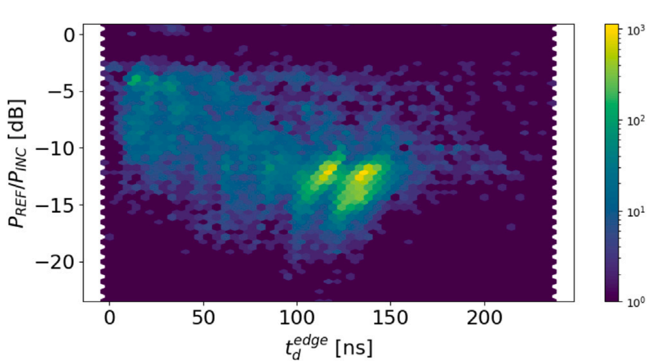

Fig. 14. 2D histogram of reflected power ratio versus t_{edge}.

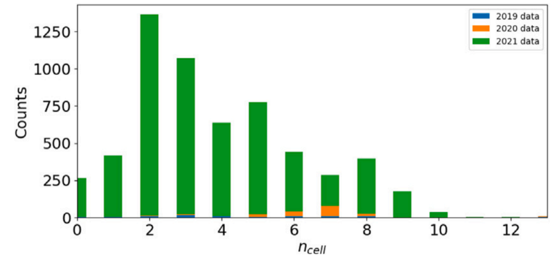

Fig. 15. BD localisation analysis for 600 ns pulse length during the conditioning process with $10\log(P_{REF}/P_{INC}) > -10$.

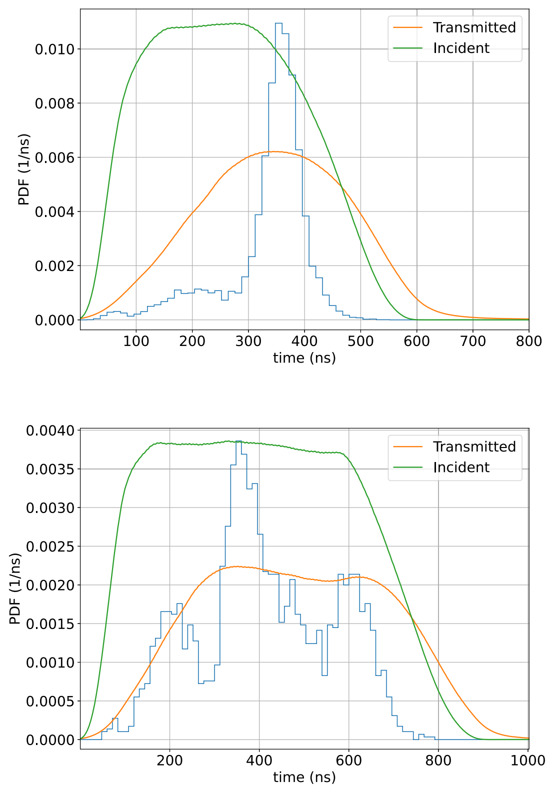

Fig. 16. BDs time occurrence inside the transmitted pulse for 600 ns (top) and 900 ns (bottom) pulse length.

Note that the shape of the transmitted pulse for a total length of 600 ns shows a higher degree of deformation, due to the fast rise time and the dispersive behaviour of the structure. As a consequence, BDs are accumulated around the maximum of the transmitted pulse, in contrast to longer pulses, where the BDs occur more uniformly along the pulse shape, as seen in Fig. 16.

Furthermore, a phase study was carried out in order to better understand whether this observed accumulation of BDs in cells 8 and 9 for short pulses is an artefact of the localisation method, as a consequence of the pulse shape deformation for short pulses, or a real BD event characterised by low reflected power.

This method is based on the comparison between the phase of the incident and reflected signal assuming that the reflection is always produced from the same location in the cell and that the BD phases from two consecutive cells are spaced $\Delta\phi = 150°$ in the BTW structure. The BD phase is computed as the difference between the phase of the reflected signal once the BD is triggered as described in [31,32],

$$\phi_{BD} = \phi_{REF}(t + t_d) - \phi_{INC}(t), \tag{7}$$

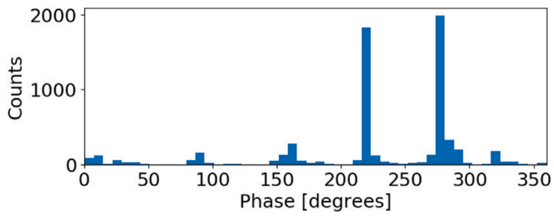

Fig. 17. Histogram of BD phases for all BDs measured.

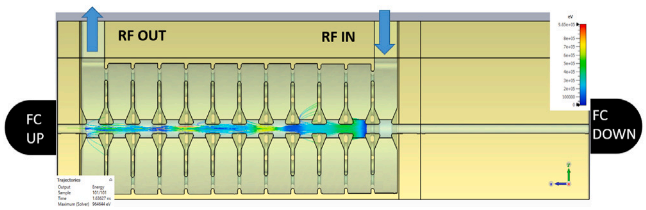

Fig. 18. 3D model of BTW S-Band cavity model in CST-PS for tracking simulations.

where ϕ_{BD} is the BD phase, $\phi_{REF}(t+t_d)$ is the phase of the reflected signal after BD and $\phi_{INC}(t)$ is the phase of the incident signal

Since the phase advance of the cavity is 150 ° per cell, a histogram of the phase of the reflected signal in a BD should show 6 peaks uniformly distributed. However, two consecutive peaks presented a higher accumulation, which is in agreement with an accumulation of BDs in two consecutive cells. This can be seen in Fig. 17.

Although the BD accumulation was observed using two independent methods, it did not stop the conditioning of the structure or caused damage to the cavity, since longer pulses were able to reach the highest power without issues. Therefore, we can conclude that, due to the deformation of the short pulses, a specific type of BD, characterised by low reflected power and specific spatial localisation, was observed during the conditioning for short pulses. Consequently, to avoid malfunctioning of the structure, it is advisable to use pulses with a rise time equivalent to the rise time of the transmitted pulse in future conditioning processes.

4. Dark current impact studies

A 3D EM model of the BTW RF accelerating cavity was developed in CST-PS [33] in order to study the dark current electron dynamics inside the cavity. In addition, the impact of the dark current on the generation of radiation, when interacting with the metallic cavity walls, was studied using Monte Carlo simulations with PENELOPE [34]. The results from these simulations were compared with experimental measurements to better understand the observed effects during the conditioning process and characterise the dark current formation and radiation generation for different operational parameters.

4.1. Dark current and radiation simulations

The 3D EM model implemented in CST-PS can be seen in Fig. 18. The two FCs in the experimental setup as seen in Fig. 3, have been included on the CST-PS model.

In CST-PS the field emission phenomenon is implemented following the Fowler–Nordheim equation [35]:

$$j_F = \frac{1.54\times10^{-6}\times10^{4.52\phi^{-0.5}}(\beta_e E)^2}{\phi}\exp\left[-\frac{6.53\times10^9\phi^{1.5}}{\beta_e E}\right], \quad (8)$$

where j_F is the current density in A/m^2, ϕ is the material work function and E is the surface electric field. First, RF fields are calculated using the high frequency solver for the structure geometry at the working frequency $f_0 = 2.9985$ GHz. Then, the electromagnetic fields are imported in the tracking module, where Fowler–Nordheim emission has been set in the irises using the copper work function $\phi = 4.5$ eV.

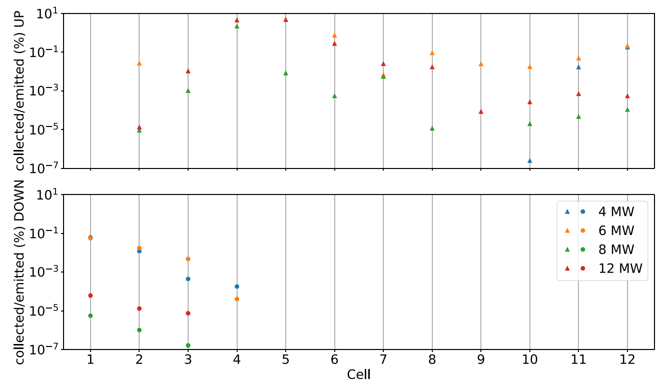

Fig. 19. Percentage of charge collected in each FC, upstream (top) and downstream (bottom), with respect to the total charge emitted per cell for two different input power.

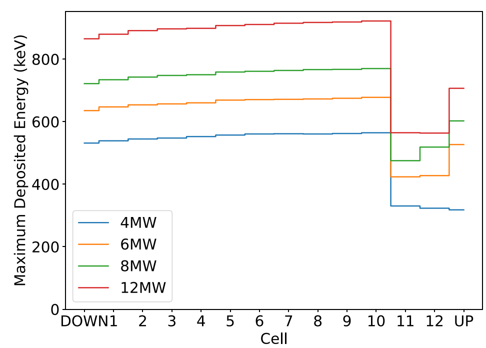

Fig. 20. Maximum energy of electrons colliding in each cell of the cavity or FC.

Afterwards, CST-PS computes the beam dynamics of the dark current electrons. The percentage of collected charge in each FC relative to the emitted charge at each cell is shown in Fig. 19. It can be seen that the number of electrons collected by the upstream FC is larger and it exhibits a more uniform distribution. In contrast, only electrons emitted from the cells near the exit beam pipe are able to reach the downstream FC, and this number decreases for higher input power. From these simulations we can conclude that electrons travelling in the downstream direction do not synchronise with the low phase velocity of the RF fields and collide with the cavity walls. Conversely, some electrons travelling in the upstream direction are able to reach further distance and can be collected in the upstream FC. These results are consistent with the experimental observations during RF conditioning, as shown in Fig. 6.

The maximum energy of the dark current electrons lost at the different cavity cells and at the FCs was studied for an input power ranging from 4 to 12 MW. The results of this study are depicted in Fig. 20. As expected, the kinetic energy of the electrons colliding with the cavity walls and reaching the FCs increases with the input power. Additionally, the value of the maximum kinetic energy recorded up to cell number 11 barely changes for a given input power since, according to the CST simulations, it corresponds to electrons travelling in the downstream direction, achieving higher energy. However, from cell number 11 onward, the electrons of maximum energy are travelling in the upstream direction, resulting in less energy gain. The maximum kinetic energy of the electrons is between 550–920 keV for P = 4–12 MW.

To estimate the impact of this dark current on the radiation reaching the exterior of the cavity, Monte Carlo simulations were performed using PENELOPE, a software based on Monte Carlo simulations for

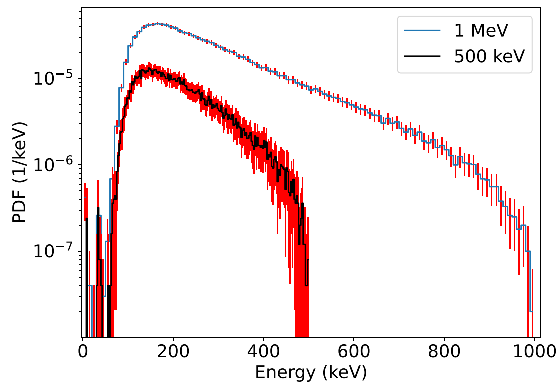

Fig. 21. Simulated bremsstrahlung spectrum from electrons colliding with a copper plane.

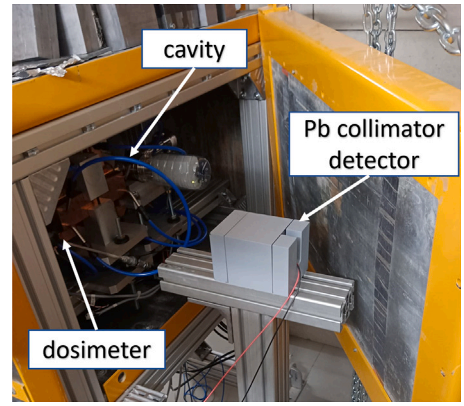

Fig. 22. Experimental set up for the bremsstrahlung photons spectrum measurements.

electrons and photons transport in matter [34]. Since electrons are light particles, their interaction with the copper walls of the cavity is dominated by bremsstrahlung [36].

In order to understand the expected energy spectrum distribution of the resulting radiation, the interaction between electrons and copper walls was simulated. The energy of the electrons simulated was chosen based on the CST-PS tracking simulation. In Fig. 21, the bremsstrahlung spectrum is shown for Cu ($Z = 29$) for electrons with kinetic energy 1 MeV and 0.5 MeV. The electron source was set as a cone beam, separated 0.5 cm from the 5 mm thick wall and a dispersion angle of 5°. The energy of the photons emitted upwards the wall, were recorded for the spectrum, and as observed, the number of photons generated is higher for higher electron energies. From this spectra one can verify the maximum energy of the incident electrons by examining the cutoff at the tail of the spectra in logarithmic scale with the horizontal axis. Therefore, by measuring the photon spectrum surrounding the cavity we can extrapolate the maximum energy of the electrons that have produced this radiation. To validate the CST-PS model in predicting the maximum energy gain by the dark current electrons, radiation energy spectrum measurements have been performed. The experimental setup and initial results are presented in the next subsection.

4.2. Radiation energy spectra measurements

During the conditioning process, the RF pulse frequency rate is between 2 and 200 Hz, and the length of the pulses is <5 μs. As shown in Fig. 10, the normalised dose during an RF pulse is on the order of 10 Gy/min, which corresponds to $\sim 10^{13}$ photons/s/sr assuming an isotropic emission. To measure the energy spectrum of this radiation without saturating the detector, a small $CeBr_3$ scintillating crystal and a lead collimation system with holes of 4 and 2 mm diameter were used to limit the amount of photons reaching the detector, as shown in Fig. 22.

In this case, a typical setup for photon detection consists of a scintillating crystal, a photomultiplier tube (PMT), a preamplifier, an amplifier, and a Multi-Channel Analyzer (MCA). For our experiment this setup cannot be used due to the slow acquisition time of the electronics, which leads to overlapping between consecutive photons due to the high photon fluence. In Fig. 23 a typical MCA signal is shown. The signal has a Gaussian shape and the photon energy is proportional to the peak value.

Here, it can be observed that the response time is on the same order of magnitude as the RF pulse length, due to the high fluence of photons, this response is not fast enough, leading to pile-up. However, if we directly measured the output signal from the PMT with an oscilloscope, the acquisition process is much faster, around 100 ns. This allows us to process several photons per RF pulse and avoid overlapping. PMT

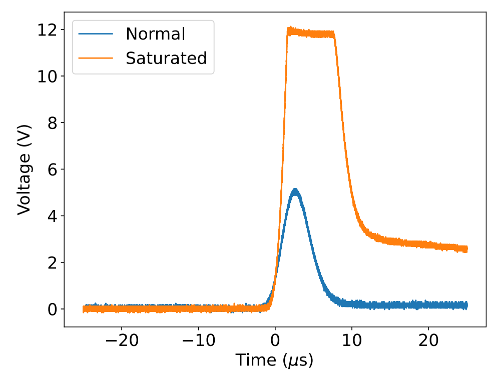

Fig. 23. Output signals from the amplifier for the detection of one photon or a saturated signal due to overlapping.

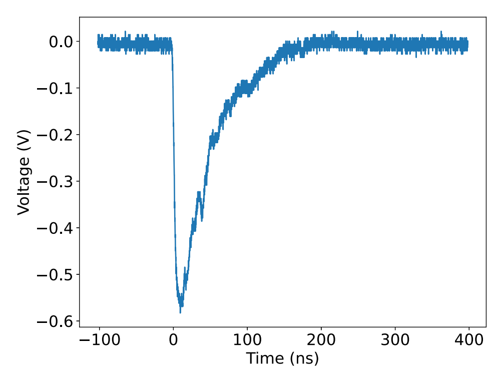

Fig. 24. Output signals from the PMT for a single photon.

signals are characterised by a rise time of 1–2 ns and an exponential decay with $\tau = 25$ ns, where the photon energy is proportional to the area. This is illustrated in Fig. 24.

Therefore, in our experimental set-up, we used an oscilloscope Teledyne LeCroy waverunner 9404M connected to the output of the PMT to collect the signals. A post processing analysis script was developed to reconstruct the photon energy spectrum.

Measurements were performed for different RF input power values ranging from 4 to 6.5 MW, and the resulting measured spectra are depicted in Fig. 25. Due to the high increase in the photon flux, the measurements were split into two sets to avoid overlapping or low measurement rate: the 4 mm collimation hole was used for $P = 4$–5 MW (top) and the 2 mm hole for higher input power (bottom).

The first observed peak in Fig. 21 corresponds to lead X-rays (~75 keV), used for the collimation system, while the continuum region

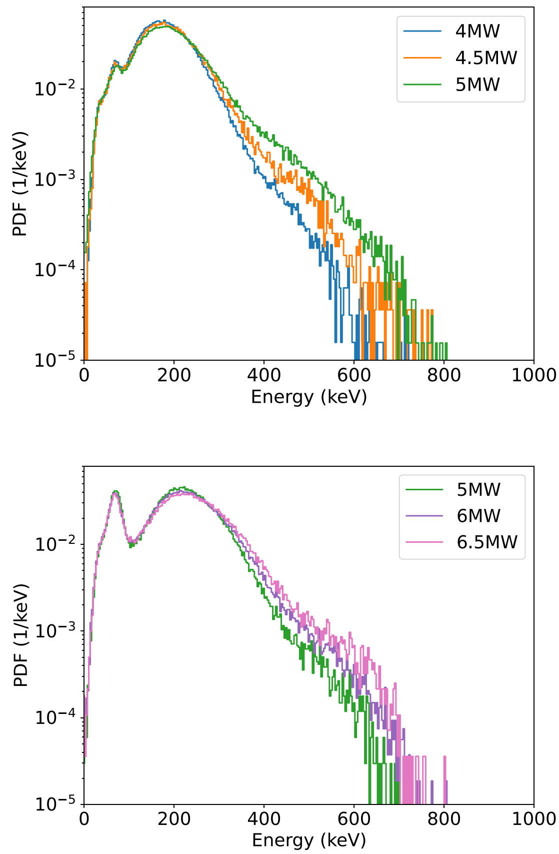

Fig. 25. Photon energy spectrum using a collimator with a hole with a diameter of 4 mm (top) and 2 mm (bottom).

of the spectra has a typical bremsstrahlung shape. As observed if we compare the top and bottom plots of Fig. 25, the bremsstrahlung peak is shifted when the smaller hole is used. Numerical simulation showed that this shift is likely due to a misalignment between the collimator hole and the incidence angle of the photons emitted from the cavity of around ∼2.8°. As a consequence, when the small hole is used, the photons must travel through a thin layer of Pb which shields more effectively the low energy photons.

From Fig. 25, the maximum energy of the source electrons can be inferred by examining the cut-off energy of the measured spectrum. As seen, the maximum energy of the photons increases with the RF input power, as expected from the simulations performed with CST-PS and PENELOPE, presented in Fig. 20. However, it can be observed that both figures predict different maximum energies for the same input power at 5 MW. This is due to overlapping of various photons at high input power caused by the high photon flux. Consequently, the small hole must be used for $P_{in} > 5$ MW.

The spectrum measurement agrees with the numerical simulation since the maximum energy increases with the input power. In addition, the measured maximum energy of the electrons is the range of 600–750 keV which is compatible with the numerical simulations that predicted a range between 550–700 keV.

5. Summary

The BTW S-band HG accelerating cavity designed by [28] has been tested for the first time up to an accelerating field of 39 MV/m, with pulses of 800 ns flat-top. A total of 950 million pulses were injected into the cavity during the conditioning and high-power tests conducted over a span of 120 days. Approximately 580 million pulses were required to attain maximum power for short pulses of 200 ns with a flat-top, while the pulse count decreased significantly for longer pulses, requiring 100 million pulses for 500 ns and 50 million for 800 ns. The conditioning process exhibited a linear correlation with the number of pulses introduced into the structure, resulting in a proportional reduction in conditioning time with an increased repetition rate. However, dark current signals displayed non-linear behaviour, eventually reaching a saturation point during the conditioning process, even as radiation dose levels continued to rise.

The evolution of the beta enhancement factor was estimated by conducting multiple scans of the dark current's dependence on the gradient at different stages of the conditioning process, revealing a hyperbolic decrease with the maximum accelerating field. Furthermore, the BDR was investigated at three different gradient levels and two distinct times. These findings align with the BDR's dependence on the electric field and demonstrate an improvement in the cavity's performance following conditioning at nominal power levels.

The study on the localisation of BD events revealed a fairly uniform distribution for pulses lasting 500 ns and 800 ns with a flat-top. However, an accumulation of BD events in cells number 8 and 9 was observed for short pulses of 200 ns. A thorough examination of these short pulses led to the conclusion that, due to their limited duration and deformation of the transmitted pulse, a specific type of BD occurred at the onset of the RF pulse decay, characterised by low reflected power. This accumulation of BD events disappeared for longer flat-top pulses and did not stop the conditioning process.

The dark current and radiation emission in the BTW accelerating structure have been modelled with a 3D EM code. The numerical study of electron dynamics associated with dark current aimed to validate the experimental results. Simulations confirmed that electrons do not synchronise with the phase velocity of the cavity, thereby preventing their collection at the Downstream FC, in agreement with experimental observations.

Additionally, the maximum kinetic energy expected for electrons is in the same order of magnitude as the maximum energy detected for bremsstrahlung photons emitted by the copper walls of the structure. The method developed for these measurements can be used to estimate the shielding needed in the operation of HG cavities where dark currents produce the emission of radiation.

6. Conclusion

The high-power tests to evaluate the performance and conditioning process of a new HG accelerating cavity design are demanding in time and require special laboratories. A better understanding and modelling of the processes involved are essential for pushing the R&D and application of the HG technology. In this paper we present the high-power tests performed to a BTW accelerating cavity at the IFIC HG laboratory. The conditioning process has been performed at a repetition rate of 300 Hz, reducing the conditioning time by a factor 10 with respect to what is used in other high-power laboratories. From these experimental tests we could conclude that the beta enhancement factor decreases during the conditioning. In addition, a strong correlation between the BD probability and the input pulse shape was observed. This observation puts requirements on the optimised pulse shape in order to be able to monitor the BD distribution inside the structure along the conditioning process.

Typically, the dark current observable is used to monitor the evolution of the conditioning process. In the presented tests, the dose is also used to monitor the evolution of the conditioning process, both quantities are reduced. On top of that, we observed a BDR improvement when operating at a constant gradient.

In terms of the design of the BTW cavity, a gradient of 35 MV/m with a $BDR < 7.7 \times 10^{-7}$ bpp/m was achieved for the first time. We observed a warming up of the cavity when high repetition rates are used. Thus, the cooling design will need to be revised in order to be able to operate at high repetition rates to reduce the conditioning process time. Moreover, the 3D EM model was validated by measurements allowing it to be used to make predictions on the shielding requirements. Furthermore, the observed energies of the emitted electron were always below material activation threshold.

CRediT authorship contribution statement

P. Martinez-Reviriego: Writing – original draft, Software, Formal analysis, Conceptualization. **N. Fuster-Martínez:** Writing – original draft, Software, Formal analysis, Conceptualization. **D. Esperante:** Writing – review & editing, Supervision, Funding acquisition, Conceptualization. **M. Boronat:** Writing – review & editing, Software, Formal analysis, Conceptualization. **B. Gimeno:** Writing – review & editing, Supervision, Funding acquisition, Conceptualization. **C. Blanch:** Writing – review & editing. **D. González-Iglesias:** Writing – review & editing. **P. Martín-Luna:** Writing – review & editing. **E. Martínez:** Writing – review & editing. **A. Menendez:** Writing – review & editing. **L. Pedraza:** Writing – review & editing. **J. Fernández:** Writing – review & editing. **J. Fuster:** Writing – review & editing, Funding acquisition. **A. Grudiev:** Writing – review & editing. **N. Catalan Lasheras:** Writing – review & editing. **W. Wuensch:** Writing – review & editing.

Declaration of competing interest

The authors declare the following financial interests/personal relationships which may be considered as potential competing interests: Pablo Martinez-Reviriego reports financial support was provided by Spain Ministry of Science and Innovation. Nuria Fuster-Martinez reports financial support was provided by Valencia Department of Education Culture and Sport. If there are other authors, they declare that they have no known competing financial interests or personal relationships that could have appeared to influence the work reported in this paper.

References

[1] C.M. Charlie Ma, Tony Lomax, Proton and Carbon Ion Therapy, CRC Press, 2012.
[2] P. Haridasan, Unscear 2013 report, Radiat. Prot. Environ. 36 (3) (2013) 143.
[3] Walter Tinganelli, Marco Durante, Carbon ion radiobiology, Cancers 12 (10) (2020) 3022.
[4] Particle therapy co-operative group, 2024, https://www.ptcog.site/index.php/facilities-under-construction. (Accessed 23 June 2024).
[5] Vittorio Bencini, Design of a Novel Linear Accelerator for Carbon Ion Therapy (Ph.D. thesis), Rome U., 2020.
[6] A. Degiovanni, U. Amaldi, R. Bonomi, M. Garlasché, A Garonna, S Verdú-Andrés, R Wegner, TERA high gradient test program of RF cavities for medical linear accelerators, Nucl. Instrum. Methods Phys. Res. A 657 (1) (2011) 55–58.
[7] S. Benedetti, A. Grudiev, A. Latina, High gradient linac for proton therapy, Phys. Rev. Accel. Beams 20 (4) (2017) 040101.
[8] Alberto Degiovanni, Giovanni De Michele, Rossana Bonomi, Francisco Cabaleiro Magallanes, Michele Caldara, Veliko Dimov, Marco Esposito, Daniel Fink, Manuel Gallas Torreira, Yevgeniy Ivanisenko, et al., Design, integration, and commissioning of the first linac for image guided hadron therapy prototype, Phys. Rev. Accel. Beams 27 (5) (2024) 054701.
[9] ADAM, 2024, https://www.avoplc.com/en-gb/. (Accessed 23 April 2024).
[10] Ugo Amaldi, Rossana Bonomi, S Braccini, M Crescenti, A Degiovanni, M Garlasché, A Garonna, G Magrin, C Mellace, P Pearce, et al., Accelerators for hadrontherapy: From lawrence cyclotrons to linacs, Nucl. Instrum. Methods Phys. Res. A 620 (2–3) (2010) 563–577.
[11] A.S. Plastun, et al., Beam dynamics studies for a compact carbon ion linac for therapy, in: Proc. of Linear Accelerator Conference (LINAC'16), East Lansing, MI, USA, 25-30 September 2016, in: Linear Accelerator Conference, number 28, JACoW, Geneva, Switzerland, 2017, pp. 946–948, http://dx.doi.org/10.18429/JACoW-LINAC2016-THPLR042, URL http://jacow.org/linac2016/papers/thplr042.pdf. https://doi.org/10.18429/JACoW-LINAC2016-THPLR042.
[12] Markus Aicheler, P Burrows, M Draper, Terence Garvey, P Lebrun, K Peach, N Phinney, H Schmickler, Daniel Schulte, N Toge, A Multi-TeV Linear Collider Based on CLIC Technology: CLIC Conceptual Design Report, Technical Report, SLAC National Accelerator Lab., Menlo Park, CA (United States), 2014.
[13] Alberto Degiovanni, Walter Wuensch, Jorge Giner Navarro, Comparison of the conditioning of high gradient accelerating structures, Phys. Rev. Accel. Beams 19 (3) (2016) 032001.
[14] Walter Wuensch, Alberto Degiovanni, Sergio Calatroni, Anders Korsbäck, Flyura Djurabekova, Robin Rajamäki, Jorge Giner-Navarro, Statistics of vacuum breakdown in the high-gradient and low-rate regime, Phys. Rev. Accel. Beams 20 (1) (2017) 011007.
[15] Andreas Kyritsakis, Mihkel Veske, Kristjan Eimre, Vahur Zadin, Flyura Djurabekova, Thermal runaway of metal nano-tips during intense electron emission, J. Phys. D: Appl. Phys. 51 (22) (2018) 225203.
[16] Jan Paszkiewicz, Studies of Breakdown and Pre-Breakdown Phenomena in High-Gradient Accelerating Structures (Ph.D. thesis), University of Oxford, 2020.
[17] William Lee Millar, Operation of Multiple Accelerating Structures in an X-Band High-Gradient Test Stand, Lancaster University (United Kingdom), 2021.
[18] Eliyahu Zvi Engelberg, Ayelet Badichi Yashar, Yinon Ashkenazy, Michael Assaf, Inna Popov, Theory of electric field breakdown nucleation due to mobile dislocations, Phys. Rev. Accel. Beams 22 (8) (2019) 083501.
[19] Eliyahu Zvi Engelberg, Jan Paszkiewicz, Ruth Peacock, Sagy Lachmann, Yinon Ashkenazy, Walter Wuensch, Dark current spikes as an indicator of mobile dislocation dynamics under intense dc electric fields, Phys. Rev. Accel. Beams 23 (12) (2020) 123501.
[20] Mihkel Veske, Andreas Kyritsakis, Flyura Djurabekova, Kyrre Ness Sjobak, Alvo Aabloo, Vahur Zadin, Dynamic coupling between particle-in-cell and atomistic simulations, Phys. Rev. E 101 (5) (2020) 053307.
[21] Ruth Peacock, et al., Pulsed DC high field measurements of irradiated and non-irradiated electrodes of different materials, JACoW LINAC2022 (2022) 441–444, http://dx.doi.org/10.18429/JACoW-LINAC2022-TUPOPA13.
[22] Catarina Da Palma Serafim, et al., Microscopy investigation on different materials after pulsed high field conditioning and low energy H^- irradiation, JACoW LINAC2022 (2022) 422–425, http://dx.doi.org/10.18429/JACoW-LINAC2022-TUPOPA06.
[23] T Argyropoulos, S Benedetti, C Blanc Gutierrez, N Catalan Lasheras, A Degiovanni, D Esperante Pereira, M Garlasche, J Giner Navarro, A Grudiev, G Mcmonagle, Fabrication and testing of a novel S-band backward travelling wave accelerating structure for proton therapy linacs, Cell 155, 150.
[24] A Vnuchenko, D Esperante Pereira, B Gimeno Martinez, S Benedetti, N Catalan Lasheras, M Garlasch, A Grudiev, G McMonagle, S Pitman, I Syratchev, et al., High-gradient testing of an S-band, normal-conducting low phase velocity accelerating structure, Phys. Rev. Accel. Beams 23 (8) (2020) 084801.
[25] SV Kutsaev, R Agustsson, S Boucher, O Chimalpopoca, D Meyer, A Murokh, B Mustapha, A Nassiri, A Yu Smirnov, T Smith, et al., Test results of a high-gradient 2.856-GHz negative harmonic accelerating waveguide, IEEE Microw. Wirel. Compon. Lett. 31 (9) (2021) 1098–1101.
[26] Nuria Catalán Lasheras, Theodoros Argyropoulos, Daniel Esperante Pereira, Cedric Eymin, Jorge Giner Navarro, Gerard McMonagle, Stephane Rey, Anastasiya Solodko, Igor Syratchev, Matteo Volpi, et al., Commissioning of xbox-3: A very high capacity X-band test stand, in: 28th Linear Accelerator Conf.(LINAC'16), East Lansing, MI, USA, 25-30 September 2016, JACOW, Geneva, Switzerland, 2017, pp. 568–571.
[27] Anna Vnuchenko, Theodoros Argyropoulos, Cesar Blanch Gutiérrez, Nuria Catalán Lasheras, Daniel Esperante Pereira, Angeles Faus-Golfe, Jorge Giner Navarro, Gerard McMonagle, Igor Syratchev, Walter Wuensch, Design and construction of a high-gradient RF lab at IFIC-valencia, in: 8th International Particle Accelerator Conference, 2017, THPIK081.
[28] Stefano Benedetti, High-Gradient and High-Efficiency Linear Accelerators for Hadron Therapy (Ph.D. thesis), Ecole Polytechnique Fédérale de Lausanne, 2018.
[29] Sagy Lachmann, Marek Jacewicz, Iaroslava Profatilova, Jan Paszkiewicz, Walter Wuensch, Yinon Ashkenazy, Statistical analysis of field-emission currents, Phys. Rev. Appl. 16 (2) (2021) 024007.
[30] Alexej Grudiev, S. Calatroni, W. Wuensch, New local field quantity describing the high gradient limit of accelerating structures, Phys. Rev. Special Top.-Accel. Beams 12 (10) (2009) 102001.
[31] Alberto Degiovanni, Benjamin Woolley, Walter Wuensch, Wilfrid Farabolini, Steffen Döbert, Igor Syratchev, Jorge Giner Navarro, Joseph Tagg, Diagnostics and Analysis Techniques for High Power X-Band Accelerating Structures, Technical Report, 2014.
[32] Andrea Palaia, Valery Dolgashev, James Lewandowski, Stephen Weathersby, Diagnostics of RF breakdowns in high-gradient accelerating structures, in: DIPAC2011, 10th European Workshop on Beam Diagnostics and Instrumentation for Particle Accelerators. 16-18 May, Hamburg, Germany, 2011, pp. 527–529.
[33] CST Studio Suite software, URL https://www.3ds.com/products-services/simulia/products/cst-studio-suite/.
[34] Francesc Salvat, José M Fernández-Varea, Josep Sempau, et al., PENELOPE-2006: A code system for Monte Carlo simulation of electron and photon transport, in: Workshop Proceedings, Vol. 4, Citeseer, 2006, p. 7.
[35] J.W. Wang, G.A. Loew, Field Emission and Rf Breakdown in High-Gradient Room Temperature Linac Structures, Technical Report, Stanford Univ., Stanford Linear Accelerator Center, CA (US), 1997.
[36] Glenn F. Knoll, Radiation Detection and Measurement, John Wiley & Sons, 2010.